

**Measurements of nonequilibrium interatomic forces using time-domain x-ray scattering**

Samuel W. Teitelbaum<sup>1,2,\*</sup>, Thomas C. Henighan<sup>1,3</sup>, Hanzhe Liu<sup>1,3</sup>, Mason P. Jiang<sup>1,3</sup>, Diling Zhu<sup>4</sup>, Matthieu Chollet<sup>4</sup>, Takahiro Sato<sup>4</sup>, Éamonn D. Murray<sup>5</sup>, Stephen Fahy<sup>6,7</sup>, Shane O'Mahony<sup>6,7</sup>, Trevor P. Bailey<sup>8</sup>, Ctirad Uher<sup>8</sup>, Mariano Trigo<sup>1,2</sup> and David A. Reis<sup>1,2</sup>

<sup>1</sup>Stanford PULSE Institute, SLAC National Accelerator Laboratory, Menlo Park, California 94025, USA

<sup>2</sup>Stanford Institute for Materials and Energy Sciences, SLAC National Accelerator Laboratory, Menlo Park, California 94025, USA

<sup>3</sup>Department of Physics, Stanford University, Stanford, California 94305, USA

<sup>4</sup>Linac Coherent Light Source, SLAC National Accelerator Laboratory, Menlo Park, California 94025, USA

<sup>5</sup>Department of Physics and Department of Materials, Imperial College London, London SW7 2AZ, United Kingdom

<sup>6</sup>Tyndall National Institute, Cork T12 R5CP, Ireland

<sup>7</sup>Department of Physics, University College Cork, Cork T12 R5CP, Ireland

<sup>8</sup>Department of Physics, University of Michigan, Ann Arbor, Michigan 48109, USA



(Received 26 January 2021; accepted 23 April 2021; published 18 May 2021)

We demonstrate an experimental approach to determining the excited-state interatomic forces using femtosecond x-ray pulses from an x-ray free-electron laser. We determine experimentally the excited-state interatomic forces that connect photoexcited carriers to the nonequilibrium lattice dynamics in the prototypical Peierls-distorted material, bismuth. The forces are obtained by a constrained least-squares fit of a pairwise interatomic force model to the excited-state phonon dispersion relation as measured by the time- and momentum-resolved x-ray diffuse scattering. We find that photoexcited carriers weaken predominantly the nearest-neighbor forces, which drives the measured softening of the transverse acoustic modes throughout the Brillouin zone as well as the zone-center  $A_{1g}$  optical mode. This demonstrates a bond-selective approach to measuring electron-phonon coupling relevant to a broad range of photoinduced phase transitions and transient light-driven states in quantum materials.

DOI: [10.1103/PhysRevB.103.L180101](https://doi.org/10.1103/PhysRevB.103.L180101)

In light-driven nonequilibrium systems, the interatomic forces can be strongly modified, either directly by creation of hot carriers [1–4] or with low-energy resonant excitations [5,6]. However, characterizing the interatomic forces in these transients is challenging. Typically, only zone-center (zero wave vector) modes are probed in the nonequilibrium state, meaning that most of the degrees of freedom are experimentally inaccessible, and thus information about the microscopic nonequilibrium interatomic forces is limited. In equilibrium, these forces can be obtained by fitting the phonon dispersion relation [7] derived from a combination of experimental probes, such as inelastic neutron scattering (INS), inelastic x-ray scattering (IXS), Raman scattering, and infrared scattering, to particular ground-state force models [8–12].

Time- and momentum-resolved x-ray diffuse scattering from photoexcited materials can reveal the *nonequilibrium* phonon dispersion relation throughout the Brillouin zone [13]. Here, we demonstrate how these data can be used to extract transient excited-state interatomic forces in the prototypical Peierls-distorted material, bismuth. The forces are extracted by fitting a Born–von Karman model to time-resolved x-ray scattering experimental data at varying laser excitation levels.

We show that changes to the phonon dispersion are driven primarily by softening of the nearest-neighbor bonds, consistent with photoexcitation partially reversing the Peierls distortion. The results are in qualitative agreement with theoretical predictions for the excited-state forces and phonon dispersion performed well over a decade ago [14]. Nonetheless, we measure a significantly higher level of softening of the acoustic branches than predicted for bismuth. More generally, our results demonstrate a method that provides direct experimental access to light-modified microscopic forces.

We performed near-IR pump, x-ray scattering probe experiments at the X-ray Pump-Probe (XPP) instrument at the Linac Coherent Light Source (LCLS) x-ray free-electron laser. The experimental details are similar to those used in Ref. [15] to measure the anharmonic decay channels of the zone-center  $A_{1g}$  phonon in photoexcited bismuth. The monochromatized x-ray pulses had a photon energy of 9.5 keV and sub-50-fs pulse duration at nominally 120-Hz repetition rate [16]. The sample was a 50-nm-thick epitaxial film of bismuth with its surface normal along the trigonal axis [perpendicular to the (111) planes in rhombohedral units]. The crystal was rotated such that the x rays propagated at a  $0.5^\circ$  grazing angle from the surface and at a  $71^\circ$  angle with respect to (211) (binary axis). The incident fluence of the nearly copropagating, 800-nm (1.55 eV) p-polarized, 65-fs-excitation laser was varied between 2.5 and 8.0 mJ/cm<sup>2</sup>. A Cornell-SLAC pixel array detector (CSPAD) [17] was used to

\*Present address: Department of Physics, Arizona State University, Tempe, AZ 85287, USA, SamuelT@asu.edu

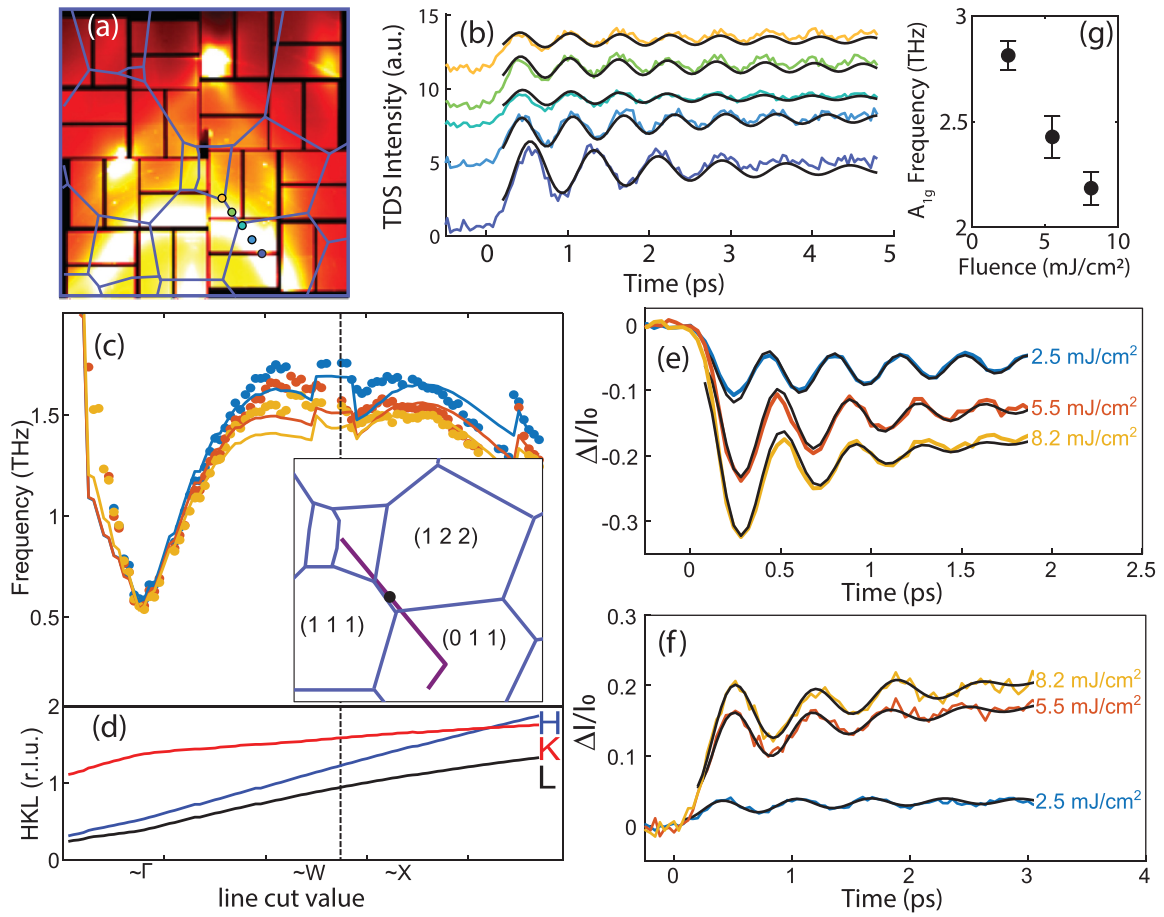


FIG. 1. (a) Diffuse scattering intensity of bismuth in our experimental geometry. (b) Representative time-resolved diffuse scattering signals at the color-coded points shown in (a) at  $2.5 \text{ mJ/cm}^2$ . (c) Observed frequencies of phonon mean-square displacements for photoexcited bismuth as a function of incident laser fluence. The data correspond to the wave vectors in (d). Solid lines show the best fits to twice the phonon frequency. The inset in (c) shows the Brillouin zones in the lower right quadrant of reciprocal space subtended by the detector in (a), and the line cut along the detector the points in (c) correspond to. The illustrated path (purple) of the line cut shown in (c) and the Brillouin zone boundaries (blue) are also indicated. (e) Time-dependent change in the Bragg intensity of the (223) peak, showing oscillations of the  $A_{1g}$  mode about its new quasiequilibrium position. (f) Time-dependent relative change in the diffuse scattering intensity for three laser fluences at the wave vector  $\mathbf{Q} = (1.00, 1.61, 1.39)$  reciprocal lattice units (r.l.u.) [black dot in the inset to (c) and dashed line in (c) and (d)]. The black lines through the data in (b), (e), and (f) correspond to the best fits as described in the text. (g) Fitted frequencies to the oscillations of the  $A_{1g}$  mode shown in (e).

simultaneously collect scattered x rays over a wide range of momentum transfer  $\hbar\mathbf{Q}$  on each x-ray pulse. The pump-probe delay was achieved via rapid scanning of the pump delay with an encoded translation stage, and time-tool correction to mitigate timing jitter between the near-IR and x-ray pulses. The shot-by-shot corrections were then assembled into a temporal array with 40 fs time spacing over a delay range of 6 ps.

The diffuse scattering depends to leading order on the  $\mathbf{Q}$ th Fourier component of the mean-square atomic displacements. In high-quality crystals the equilibrium diffuse scattering signal  $I(\mathbf{Q})$  is largely due to thermal phonons. Upon ultrafast photoexcitation, the initially thermally occupied phonons adjust to the new interatomic forces, leading to oscillations in their mean-square displacements at twice the excited-state phonon frequency. Before the phonons rethermalize, the nonequilibrium diffuse intensity  $I(\mathbf{Q}, t)$  shows oscillations in time at twice the phonon frequencies for  $\mathbf{Q}$  far from the Bragg condition [13,18].

Thus extraction of the interatomic forces from the experimental data involves three steps: First, the phonon frequencies as a function of momentum transfer are extracted by fitting a sum of damped cosine functions to the measured  $I(\mathbf{Q}, t)$ . Second, these extracted frequencies are assigned to phonons of a particular wave vector and branch. The observed oscillation frequency at each pixel was assigned to a particular phonon branch with the highest computed equilibrium thermal diffuse scattering (TDS) intensity [19,20]. This assignment assumes similar excitation amplitude relative to equilibrium for all phonon modes, such that the oscillation amplitude is proportional to the initial mean-square displacement of the mode. Finally, the interatomic forces are determined by a least-squares optimization of the Born-von Karman model parameters to the experimental data.

Figure 1 illustrates how we obtain the phonon frequencies from  $I(\mathbf{Q}, t)$ . The equilibrium diffuse scattering is shown in Fig. 1(a), showing that our reciprocal space coverage spans

multiple Brillouin zones. Each pixel on the detector maps to a unique  $\mathbf{Q}$ , each of which is mapped to a given wave vector  $\mathbf{q} = \mathbf{Q} - \mathbf{G}$  within the Brillouin zone, where  $\mathbf{G}$  is the nearest reciprocal lattice vector to  $\mathbf{Q}$ . Representative traces of  $I(\mathbf{Q}, t)$  are shown in Fig. 1(b). For each pixel we fit a sum of exponential decay and decaying cosine functions to the measured  $I(\mathbf{Q}, t)$  by linear prediction fitting [21]. Although there are six phonon branches in bismuth, we find that the data can be represented with three damped harmonic oscillators [22]. Figure 1(c) shows the dominant frequency from the fits along the reciprocal space path shown in Figs. 1(c) and 1(d) for three different excitation fluences. Also shown is the result of the best fit of our model to the data as described in more detail below.

The final step in extracting the interatomic forces is to fit a model of the phonon dispersion relation to the phonon frequencies as a function of  $\mathbf{q}$ . We model the phonon dispersion relation using a Born–von Karman model, which takes the interatomic forces as pairwise harmonic interactions between the atoms. These models are well established and, in particular, have been used successfully to interpret equilibrium phonon dispersion in bismuth measured by inelastic neutron scattering [23]. We note that modern density functional perturbation theory (DFPT) based calculations of the phonon dispersion in bismuth are also in good agreement with the neutron scattering data [14].

The pairwise forces in our model  $\Phi_{ij}^{\alpha,\beta}$  are the second derivatives of the total energy  $E$  with respect to a pair of atomic displacements  $u_i$  and  $u_j$  in directions  $\alpha$  and  $\beta$ .

Each  $\Phi_{ij}^{\alpha,\beta}$  corresponds to the force on atom  $j$  in direction  $\beta = (x, y, z)$  produced by a displacement of atom  $i$  in direction  $\alpha$ . The phonon dispersion is obtained from the dynamical matrix [7], which is the Fourier transform over the force constants

$$D_{ij}^{\alpha,\beta}(\mathbf{q}) = \frac{1}{M} \sum_{ij} \Phi_{ij}^{\alpha,\beta} e^{-i\mathbf{q}\cdot(\mathbf{r}_i - \mathbf{r}_j)}. \quad (1)$$

The factor  $M$  is the mass of the bismuth atom. The eigenvalues and eigenvectors of the dynamical matrix at wave vector  $\mathbf{q}$  are the square of the harmonic phonon normal mode frequencies  $\omega_i^2(\mathbf{q})$ , and phonon polarization  $\epsilon_i(\mathbf{q})$ , respectively.

As a starting point for the fit, we use real-space forces derived from a DFPT calculation. We limit the real-space forces to a  $4 \times 4 \times 4$  supercell, corresponding to 1152 force constants for 128 atom pairs. Additional symmetries of the crystal (rhombohedral crystal with an  $R\bar{3}m$  space group) reduce this number to 21 independent  $3 \times 3$  force matrices. Furthermore, we assume that the photoexcitation does not change the overall bonding directions of the system significantly. The assumption implies that the eigenvalues, but not the eigenvectors, of each real-space force matrix change, further reducing the adjustable forces to three per symmetry-inequivalent atom pair. This fitting procedure is equivalent to a reduced Born–von Karman model [7] where the eigenvectors of the interatomic force matrices are known. Note that though the *real-space* eigenvectors of the force matrix are fixed, the eigenvectors of the *reciprocal space* matrix (the dynamical matrix) are not fixed, meaning that the phonon polarizations

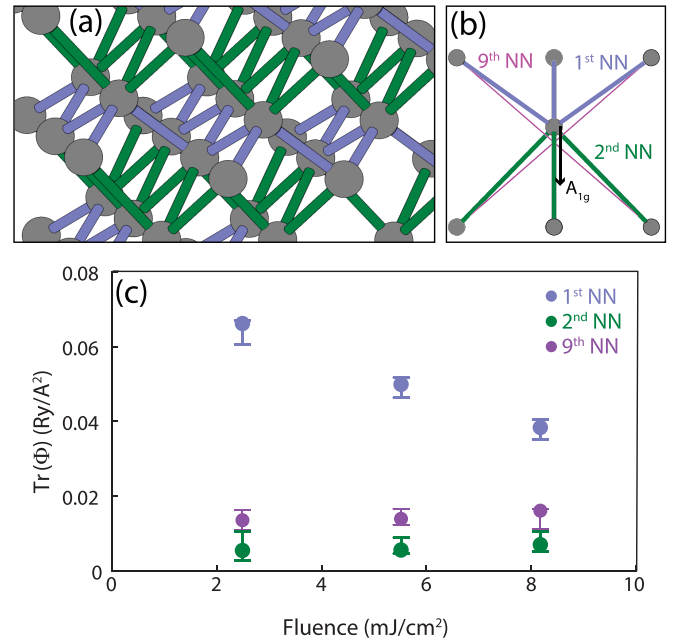


FIG. 2. (a) Illustration of the crystal structure of bismuth, with key bonds in the model highlighted. Blue and green bonds are the first- and second-nearest-neighbor bonds used in the model. The ninth-nearest-neighbor bonds connect the second-nearest neighbors in the chain direction. (b) Illustration of the nearly sixfold coordinated bonding cluster around a Bi atom (highlighted), showing the three bonds [first-, second-, and ninth-nearest neighbors (NNs)] used in the fit. The direction of the  $A_{1g}$  mode ([111] direction) is shown. (c) Traces of force matrices of the three largest interatomic forces as a function of fluence, for atom pairs illustrated in (b).

are allowed to change, restricted only by the symmetry of the real-space forces.

The eigenvectors of the real-space force matrix correspond to the directions where the restoring force applied is parallel to the atom displacement. Typically, this corresponds to one component along the bond axis, one component in the bonding plane, and one component out of the bonding plane. Of the 21 unique force matrices, we find good results if we restrict our fits for the nonequilibrium case to the three matrices with the largest trace, which correspond to the nearest-neighbor, second-nearest-neighbor, and ninth-nearest-neighbor bonds. These three bonds form along the quasi-one-dimensional (quasi-1D) Peierls chains, illustrated in Figs. 2(a) and 2(b). The other forces are kept at the values obtained by DFPT calculations.

We incorporate one more piece of experimental information into our model: the frequency of the zone-center  $LO(A_{1g})$  mode observed near the Bragg peaks [1,24]. This is analogous to including Raman scattering results as a constraint in fitting INS or IXS data to a dispersion [9]. The  $A_{1g}$  frequency was incorporated as an additional term in the optimization function and was weighted as highly as the total mean-square error from the acoustic phonon branches.

As described above, we find that adjusting three interatomic force matrices was sufficient to optimize the least-squares fit and introducing additional adjustable forces to the fitting did not significantly improve the fit. The three

forces used in the fitting are the largest three forces in the DFPT ground-state calculations and correspond to the first-, second-, and ninth-nearest neighbors, i.e., the first-, second-, and third-nearest neighbors along the nearly cubic bonding direction [Fig. 2(b)]. The Supplemental Material provides additional details about the fitting procedure, optimization function, model, and fit convergence [22].

Systematic uncertainties in this experiment arise predominantly from the geometry calibration, which introduces an uncertainty in the mapping of each detector pixel to reduced wave vector  $q$ . These systematic uncertainties are estimated by varying the crystal alignment  $\pm 1^\circ$  with respect to the trigonal axis in the fitting routine and performing the fit multiple times. The error bars in Fig. 2(c) indicate the largest and smallest fit results produced by the fitting routine over the range of possible geometries.

Further discussion of the implications of our fitting results requires discussion of the basic structure and physics of bismuth. At ambient temperature and pressure, bismuth has a Peierls-distorted rhombohedral structure with a primitive basis of two atoms per unit cell. This structure can be thought of as a rhombohedral distorted simple cubic structure, with three nearest-neighbor bonds connecting atoms into layers of buckled chains orthogonal to the trigonal axis. Photoexcitation weakens the interatomic forces and drives atoms towards a more symmetric sixfold-coordinated structure, along the  $A_{1g}$  mode coordinate [14,25–27]. In this high-symmetry structure, the green and blue bonds shown in Figs. 2(a) and 2(b) are equivalent. This motion can be observed in time-resolved optical reflectivity [25,27–29] and in x-ray diffraction [1,24,26]. Here, we discuss how photoexcitation weakening the Peierls distortion manifests in the interatomic forces and phonon dispersion relation.

The traces of the first-, second-, and ninth-nearest-neighbor excited-state force matrices extracted from our fits are shown in Fig. 2(c) as a function of fluence. The first-nearest-neighbor force has the largest change with fluence. Intuitively, this force can be thought of as arising from the bonds responsible for the Peierls distortion (dimerization of Bi atoms, accompanied by opening of a gap at the Fermi surface). When this bond is sufficiently weakened, the crystal transitions into a high-symmetry phase [25,28]. At 8 mJ/cm<sup>2</sup>, this force is already weakened to almost 50% of its ground-state value. This force constant dominates the frequency of the  $A_{1g}$  mode. As a result, at this fluence, the  $A_{1g}$  mode is softened from 2.95 to 2 THz (a 30% reduction in frequency). Extrapolating to high fluence, this force constant would go to zero at a fluence of 16 mJ/cm<sup>2</sup>, which is in agreement with theoretical and experimental evidence for where the Peierls distortion vanishes [25,28].

In the force matrix with the second largest trace [Fig. 2(b), ninth-nearest neighbor], the forces along the bonding direction stiffen slightly with increasing fluence, though it is within our experimental uncertainty. The force matrix with the third largest trace, while improving the fit, does not change appreciably with increasing fluence within the uncertainties of our fitting procedure. Modifying additional forces beyond the third and fourth strongest does not significantly improve the fit quality.

Using the fitted interatomic forces, we reconstruct the phonon dispersion along high-symmetry directions, shown

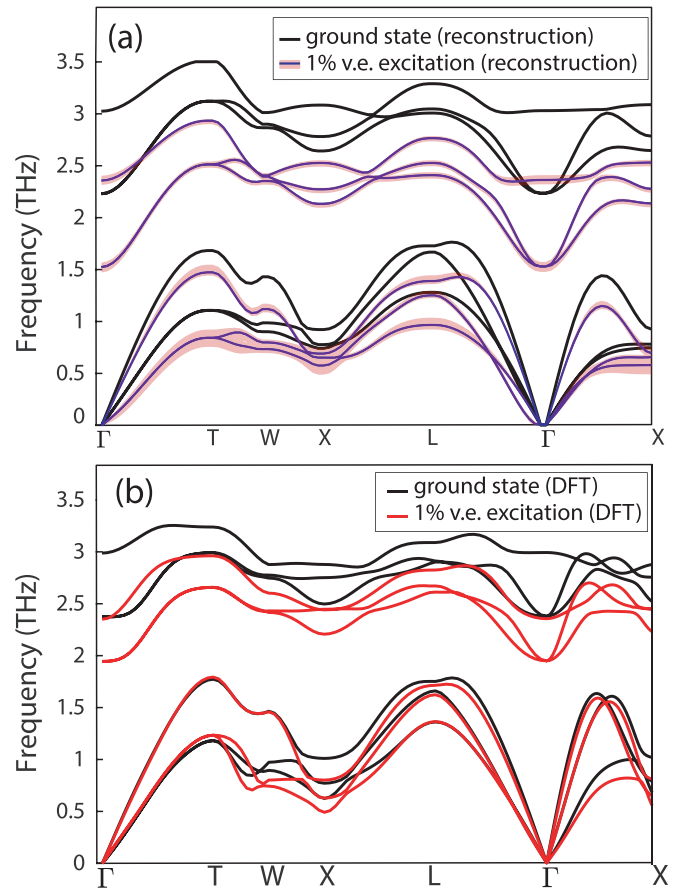


FIG. 3. (a) Reconstructed phonon dispersion along the high-symmetry directions in bismuth. Black lines show the (extrapolated) ground-state dispersion, and blue lines show the photoexcited dispersion at 5.5 mJ/cm<sup>2</sup>. Pink shaded areas indicate systematic uncertainties in the dispersion relation as described in the text. (b) DFPT calculations of the ground-state and excited-state forces for the same excitation level as in (a). v.e., valence excitation.

in Fig. 3(a), and compare with previous excited-state DFPT results from more than a decade ago [14], shown in Fig. 3(b). The shaded areas in Fig. 3(a) indicate uncertainties in the excited-state dispersion based on systematic propagation of the uncertainties in the extracted forces. We note that the softening of the acoustic modes is more pronounced than that predicted by the constrained density functional theory (DFT) calculations in Ref. [14], especially for the transverse acoustic (TA) mode near the  $L$  point. Our fits to experimental data show less softening in the ninth-nearest-neighbor force compared with excited-state DFPT predictions. Hardening of this force serves to counteract the effect of softening of the nearest-neighbor force of the acoustic modes. This explains the disagreement between our reconstruction and DFPT calculations and suggests that DFPT calculations may overestimate the photoinduced hardening of the ninth-nearest-neighbor force. This illustrates the detailed bond information contained in the nonequilibrium dispersion relation.

In conclusion, we have demonstrated a method for determining the excited-state interatomic forces using wave-vector-resolved femtosecond x-ray scattering. Time-domain experiments enable high-resolution measurements of the

phonon frequencies in the transient state. In the case of bismuth, we determine the connection between photoexcitation and the interatomic forces that drive the Peierls distortion. More generally, we anticipate that this approach could elucidate the microscopic details of nonequilibrium states beyond what is possible from time-resolved diffraction data alone. Our approach allows us to measure the influence of photoexcitation on specific chemical bonds. This will provide an invaluable tool for revealing the microscopic interactions responsible for the novel functionality of nonequilibrium materials [5,6,30–34] and provide a path towards rational design of nonequilibrium properties.

The authors thank Roberto Merlin for insightful discussions on the manuscript. This work was supported by the

U.S. Department of Energy, Office of Science, Office of Basic Energy Sciences, through the Division of Materials Sciences and Engineering under Contract No. DE-AC02-76SF00515. C.U. and T.P.B. acknowledge support from the U.S. Department of Energy, Office of Basic Energy Sciences, under Award No. DE-SC-0008574. Work at the Tyndall National Institute was supported by Science Foundation Ireland Award No. 12/IA/1601 and Irish Research Council Award No. GOIPG/2015/2784. Measurements were carried out at the Linac Coherent Light Source, a national user facility operated by Stanford University on behalf of the U.S. Department of Energy, Office of Basic Energy Sciences. Preliminary measurements were performed at the Stanford Synchrotron Radiation Lightsource (Beamline 7-2), SLAC National Accelerator Laboratory.

- 
- [1] D. M. Fritz, D. A. Reis, B. Adams, R. A. Akre, J. Arthur, C. Blome, P. H. Bucksbaum, A. L. Cavalieri, S. Engemann, S. Fahy, R. W. Falcone, P. H. Fuoss, K. J. Gaffney, M. J. George, J. Hajdu, M. P. Hertlein, P. B. Hillyard, M. Horn-von Hoegen, M. Kammler, J. Kaspar *et al.*, *Science* **315**, 633 (2007).
- [2] P. Beaud, A. Caviezel, S. O. Mariager, L. Rettig, G. Ingold, C. Dornes, S.-W. Huang, J. A. Johnson, M. Radovic, T. Huber, T. Kubacka, A. Ferrer, H. T. Lemke, M. Chollet, D. Zhu, J. M. Glowina, M. Sikorski, A. Robert, H. Wadati, M. Nakamura *et al.*, *Nat. Mater.* **13**, 923 (2014).
- [3] F. Schmitt, P. S. Kirchmann, U. Bovensiepen, R. G. Moore, L. Rettig, M. Krenz, J.-H. Chu, N. Ru, L. Perfetti, D. H. Lu, M. Wolf, I. R. Fisher, and Z.-X. Shen, *Science* **321**, 1649 (2008).
- [4] A. M. Lindenberg, J. Larsson, K. Sokolowski-Tinten, K. J. Gaffney, C. Blome, O. Synnergren, J. Sheppard, C. Caleman, A. G. MacPhee, D. Weinstein, D. P. Lowney, T. K. Allison, T. Matthews, R. W. Falcone, A. L. Cavalieri, D. M. Fritz, S. H. Lee, P. H. Bucksbaum, D. A. Reis, J. Rudati *et al.*, *Science* **308**, 392 (2005).
- [5] M. Först, C. Manzoni, S. Kaiser, Y. Tomioka, Y. Tokura, R. Merlin, and A. Cavalleri, *Nat. Phys.* **7**, 854 (2011).
- [6] D. N. Basov, R. D. Averitt, and D. Hsieh, *Nat. Mater.* **16**, 1077 (2017).
- [7] M. Born and K. Huang, *Dynamical Theory of Crystal Lattices*, Oxford Classic Texts in the Physical Sciences (Oxford University Press, Oxford, 1954).
- [8] B. N. Brockhouse and A. T. Stewart, *Phys. Rev.* **100**, 756 (1955).
- [9] R. A. Cowley, *Phys. Rev.* **134**, A981 (1964).
- [10] A. Q. R. Baron, in *Synchrotron Light Sources and Free-Electron Lasers: Accelerator Physics, Instrumentation and Science Applications*, edited by E. Jaeschke, S. Khan, J. R. Schneider, and J. B. Hastings (Springer, Cham, 2014), pp. 1721–1757.
- [11] A. Q. R. Baron, in *Synchrotron Light Sources and Free-Electron Lasers: Accelerator Physics, Instrumentation and Science Applications*, edited by E. Jaeschke, S. Khan, J. R. Schneider, and J. B. Hastings (Springer, Cham, 2014), pp. 1643–1719.
- [12] M. Krisch and F. Sette, in *Light Scattering in Solid IX*, edited by M. Cardona and R. Merlin (Springer, Berlin, 2007), pp. 317–370.
- [13] M. Trigo, M. Fuchs, J. Chen, M. P. Jiang, M. Cammarata, S. Fahy, D. M. Fritz, K. Gaffney, S. Ghimire, A. Higginbotham, S. L. Johnson, M. E. Kozina, J. Larsson, H. Lemke, A. M. Lindenberg, G. Ndabashimiye, F. Quirin, K. Sokolowski-Tinten, C. Uher, G. Wang *et al.*, *Nat. Phys.* **9**, 790 (2013).
- [14] É. D. Murray, S. Fahy, D. Prendergast, T. Ogitsu, D. M. Fritz, and D. A. Reis, *Phys. Rev. B* **75**, 184301 (2007).
- [15] S. W. Teitelbaum, T. Henighan, Y. Huang, H. Liu, M. P. Jiang, D. Zhu, M. Chollet, T. Sato, E. D. Murray, S. Fahy, S. O’Mahony, T. P. Bailey, C. Uher, M. Trigo, and D. A. Reis, *Phys. Rev. Lett.* **121**, 125901 (2018).
- [16] M. Chollet, R. Alonso-Mori, M. Cammarata, D. Damiani, J. Defever, J. T. Delor, Y. Feng, J. M. Glowina, J. B. Langton, S. Nelson, K. Ramsey, A. Robert, M. Sikorski, S. Song, D. Stefanescu, V. Srinivasan, D. Zhu, H. T. Lemke, and D. M. Fritz, *J. Synchrotron Radiat.* **22**, 503 (2015).
- [17] S. Herrmann, S. Boutet, B. Duda, D. Fritz, G. Haller, P. Hart, R. Herbst, C. Kenney, H. Lemke, M. Messerschmidt, J. Pines, A. Robert, M. Sikorski, and G. Williams, *Nucl. Instrum. Methods Phys. Res. Sect. A* **718**, 550 (2013).
- [18] T. Henighan, M. Trigo, M. Chollet, J. N. Clark, S. Fahy, J. M. Glowina, M. P. Jiang, M. Kozina, H. Liu, S. Song, D. Zhu, and D. A. Reis, *Phys. Rev. B* **94**, 020302(R) (2016).
- [19] R. Xu and T. C. Chiang, *Z. Kristallogr.* **220**, 1009 (2005).
- [20] C. B. Walker, *Phys. Rev.* **103**, 547 (1956).
- [21] H. Barkhuijsen, R. de Beer, W. Bovée, and D. van Ormondt, *J. Magn. Reson. (1969–1992)* **61**, 465 (1985).
- [22] See Supplemental Material at <http://link.aps.org/supplemental/10.1103/PhysRevB.103.L180101> for a map of the fitted frequencies on the detector and the fitting convergence as a function of the number of forces used in the reconstruction.
- [23] J. L. Yarnell, J. L. Warren, R. G. Wenzel, and S. H. Koenig, *IBM J. Res. Dev.* **8**, 234 (1964).
- [24] K. Sokolowski-Tinten, C. Blome, J. Blums, A. Cavalleri, C. Dietrich, A. Tarasevitch, I. Uschmann, E. Förster, M. Kammler, M. Horn-von Hoegen, and D. von der Linde, *Nature (London)* **422**, 287 (2003).
- [25] É. D. Murray, D. M. Fritz, J. K. Wahlstrand, S. Fahy, and D. A. Reis, *Phys. Rev. B* **72**, 060301(R) (2005).

- [26] S. L. Johnson, P. Beaud, E. Vorobeva, C. J. Milne, É. D. Murray, S. Fahy, and G. Ingold, *Phys. Rev. Lett.* **102**, 175503 (2009).
- [27] T. K. Cheng, S. D. Brorson, A. S. Kazeroonian, J. S. Moodera, G. Dresselhaus, M. S. Dresselhaus, and E. P. Ippen, *Appl. Phys. Lett.* **57**, 1004 (1990).
- [28] S. W. Teitelbaum, T. Shin, J. W. Wolfson, Y.-H. Cheng, I. J. Porter, M. Kandyla, and K. A. Nelson, *Phys. Rev. X* **8**, 031081 (2018).
- [29] M. Hase, K. Mizoguchi, H. Harima, S.-I. Nakashima, and K. Sakai, *Phys. Rev. B* **58**, 5448 (1998).
- [30] M. Mitrano, A. Cantaluppi, D. Nicoletti, S. Kaiser, A. Perucchi, S. Lupi, P. Di Pietro, D. Pontiroli, M. Riccò, S. R. Clark, D. Jaksch, and A. Cavalleri, *Nature (London)* **530**, 461 (2016).
- [31] C. W. Nicholson, A. Lücke, W. G. Schmidt, M. Puppín, L. Rettig, R. Ernstorfer, and M. Wolf, *Science* **362**, 821 (2018).
- [32] M. Chávez-Cervantes, G. E. Topp, S. Aeschlimann, R. Krause, S. A. Sato, M. A. Sentef, and I. Gierz, *Phys. Rev. Lett.* **123**, 036405 (2019).
- [33] T. Frigge, B. Hafke, T. Witte, B. Krenzer, C. Streubühr, A. Samad Syed, V. Mikšić Trontl, I. Avigo, P. Zhou, M. Ligges, D. von der Linde, U. Bovensiepen, M. Horn-von Hoegen, S. Wippermann, A. Lücke, S. Sanna, U. Gerstmann, and W. G. Schmidt, *Nature (London)* **544**, 207 (2017).
- [34] A. Kogar, A. Zong, P. E. Dolgirev, X. Shen, J. Straquadine, Y.-Q. Bie, X. Wang, T. Rohwer, I.-C. Tung, Y. Yang, R. Li, J. Yang, S. Weathersby, S. Park, M. E. Kozina, E. J. Sie, H. Wen, P. Jarillo-Herrero, I. R. Fisher, X. Wang *et al.*, *Nat. Phys.* **16**, 159 (2020).